


Article

RuCu Nanorod Arrays Synergistically Promote Efficient Water-Splitting

Tao Chen ¹, Xiangkai Kong ^{1,2,*}  and Qiangchun Liu ^{1,*}¹ School of Physics and Electronic Information, Huaibei Normal University, Huaibei 235000, China² School of Materials and Physics, China University of Mining and Technology, Xuzhou 221116, China

* Correspondence: xkong@cumt.edu.cn (X.K.); qchliu@chnu.edu.cn (Q.L.)

Abstract: In the realm of green hydrogen energy, utilizing ruthenium (Ru) as a precious metal electrocatalyst for the hydrogen evolution reaction (HER) instead of platinum (Pt/C) is an excellent choice. Unfortunately, there are not enough active sites or electronic structures on a single Ru-based catalyst to significantly improve the oxygen evolution reaction (OER). Therefore, creating bifunctional water electrolysis catalysts that are stable and highly active in a variety of media continues to be a major challenge. The study describes a new method for creating an electrocatalyst (RuCuCl/NF-2) by using Ru to regulate an inert CuCl precursor. The enhanced mass transfer performance of the distinctive coral structure and the synergistic effect of RuCu emphasize its excellent water electrolysis activity, which is based on the self-assembly of Cu nanoparticles into a conical membrane structure. Over-taking the commercial benchmark Pt/C (~38 mV to reach 10 mA cm⁻²), the RuCuCl/NF-2 displays HER activity (~25 mV to reach 10 mA cm⁻²) in 1M KOH. This sheds light on how to create more sophisticated bifunctional electrocatalysts.

Keywords: ruthenium; water splitting; oxygen evolution; hydrogen evolution; electrocatalysis



Academic Editor: Edward G. Gillan

Received: 17 December 2024

Revised: 2 January 2025

Accepted: 16 January 2025

Published: 20 January 2025

Citation: Chen, T.; Kong, X.; Liu, Q. RuCu Nanorod Arrays Synergistically Promote Efficient Water-Splitting. *Catalysts* **2025**, *15*, 98. <https://doi.org/10.3390/catal15010098>

Copyright: © 2025 by the authors. Licensee MDPI, Basel, Switzerland. This article is an open access article distributed under the terms and conditions of the Creative Commons Attribution (CC BY) license (<https://creativecommons.org/licenses/by/4.0/>).

1. Introduction

Hydrogen energy is considered to be an outstanding green energy with considerable development potential due to its wide distribution, high calorific value and minimal pollution [1–3]. Electrolyzed water is one of the many green hydrogen generation techniques that has drawn a lot of attention due to its low cost, high product purity and pollution-free manufacturing, which may help with energy crisis resolution and carbon neutrality [4–7]. Electrochemical water splitting consists of two half-reactions: the hydrogen evolution reaction (HER) at the cathode and the oxygen evolution reaction (OER) at the anode [8]. However, the general application of water electrolysis is severely limited by the slow kinetics of the anodic oxygen evolution reaction [9].

Although noble metal-based electrocatalysts, such as platinum (Pt) and iridium (Ir), exhibit high catalytic activity, their limited stability, high cost and scarce availability pose significant challenges to their widespread application and research [10–13]. Therefore, Ru-based materials have started to attract attention due to their superior electrochemical activity, relatively abundant availability and lower cost compared to Ir [14]. As a result, the development and production of highly stable and cost-effective Ru-based electrocatalysts, aimed at minimizing electrode potentials and energy consumption during the water electrolysis process, has become a new direction for efficient hydrogen production [15–17]. An excellent water electrolysis performance in both alkaline and neutral media is difficult

to achieve despite the fact that Cu-based compound electrolysis catalysts have been the subject of several investigations [18]. In particular, there is a limited number of studies on copper-based HER catalysts. As such, the design of high-performance copper-based electrocatalysts presents both a significant opportunity and a formidable challenge [19–21]. One effective method for changing the electronic structure of precursor metals, strengthening hydrogen atomic bonds and increasing their intrinsic catalytic capacity is multi-component collaborative engineering [22–24]. Recent studies have focused extensively on modifying the electronic structure of precursor metals by incorporating additional elements to enhance H* bonding and improve their intrinsic catalytic activity [25]. The Ru–H bond strength is comparable to that of platinum–H bonds, which has piqued interest in ruthenium-based electrocatalysts, which are cheap and abundant in deposits [26,27]. Previous studies have shown that ruthenium, as a modulator to optimize ΔGH^* , is an ideal alternative for competitive catalytic performance [28]. Based on the foregoing, the use of Ru to modulate Cu-based catalysts has emerged as a highly promising and viable strategy.

Building on this concept, this paper created a brand-new, highly effective RuCuCl/NF-2 electrocatalyst that uses a CuCl precursor, a programmable annealing method, and continuous cleaning and environmental control during the production process. Ru nanoparticles offer a rich synergistic contact with uniformly distributed CuCl substrates. Ru and Cu work in concert to give RuCuCl/NF-2 high HER activity and stability in alkaline environments. RuCuCl/NF-2 needs a Tafel slope of 21.9 mV dec⁻¹ and an overpotential of about 25 mV to reach a current density of 10 mA cm⁻².

2. Results and Discussion

2.1. Catalyst Synthesis and Characterization

In this study, a rapid and easy immersion method was used to create an inexpensive CuCl at room temperature (Figure 1a). Put simply, certain amounts of hydrochloric acid and copper sulfate are dissolved in deionized water. After spending varied lengths of time submerged in the reaction solution, the nickel foam is rinsed and vacuum-dried at room temperature. This approach uses nickel foam as a conductive substrate and matrix due to its comparatively low cost and scalable pore structure. Although certain integrated copper-based catalytic electrodes have been described, nothing is known about the usage of CuCl as a precursor to create bifunctional water electrolysis catalysts. Most of these electrodes are made from Cu(OH)₂ nanorod arrays that have already been manufactured. In order to deposit Cu species on the nickel foam substrate, free Cu ions can be collected and immobilized using HCl as CuCl is insoluble in aqueous solution at room temperature.

The end product copper-based catalyst will therefore be suited for direct use as an electrolytic electrode, and CuCl thin films are expected to form an ordered copper-based nanoarray on the substrate. This approach is scalable and economical. In further research, ruthenium and the produced CuCl catalyst were subjected to regulated annealing, and it was found that a small amount of Ru could greatly enhance the CuCl precursor's water electrolyzed performance [29]. Powder X-ray diffraction (XRD) was used to look into how the metal phase changed as CuCl/NF and RuCuCl/NF-2 were produced. With the exception of the inevitable Ni-foam diffraction peak (PDF#04-0850), the XRD pattern (Figure 1b) and Figure S1 demonstrate that all other diffraction peaks may be indexed as Ru (PDF#06-0663) and CuCl (PDF#06-0344). It is possible that the freshly formed Ru phase will influence catalytic activity more. Additionally, we looked at the XRD of three CuCl precursors with various morphologies and processing times. As can be seen in Figure S2, these CuCl precursors had very similar Cu-based crystal structures, proving that CuCl precursors could be successfully synthesized at various reaction times. The XRD peaks of RuCuCl/NF-2 and RuCuCl/NF-3 catalysts were observed in Figure S3,

and the RuCu catalysts were successfully prepared. The amorphous carbon peak in the (002) plane at around 23° is probably caused by the porous structure of the nickel foam. Certain X-ray diffraction peaks are able to pass through the nickel foam and land on the test plate. CuCl/NF only shows CuCl and Ni diffraction peaks. Ru's (100) and (002) facets are indicated by diffraction peak centers at approximately 38.387° and 42.152° , respectively, according to the XRD examination of RuCuCl/NF-2 samples. In other words, CuCl/NF was modified to include a controlled annealing process along with a new catalyst for the successful creation of composite Ru components.

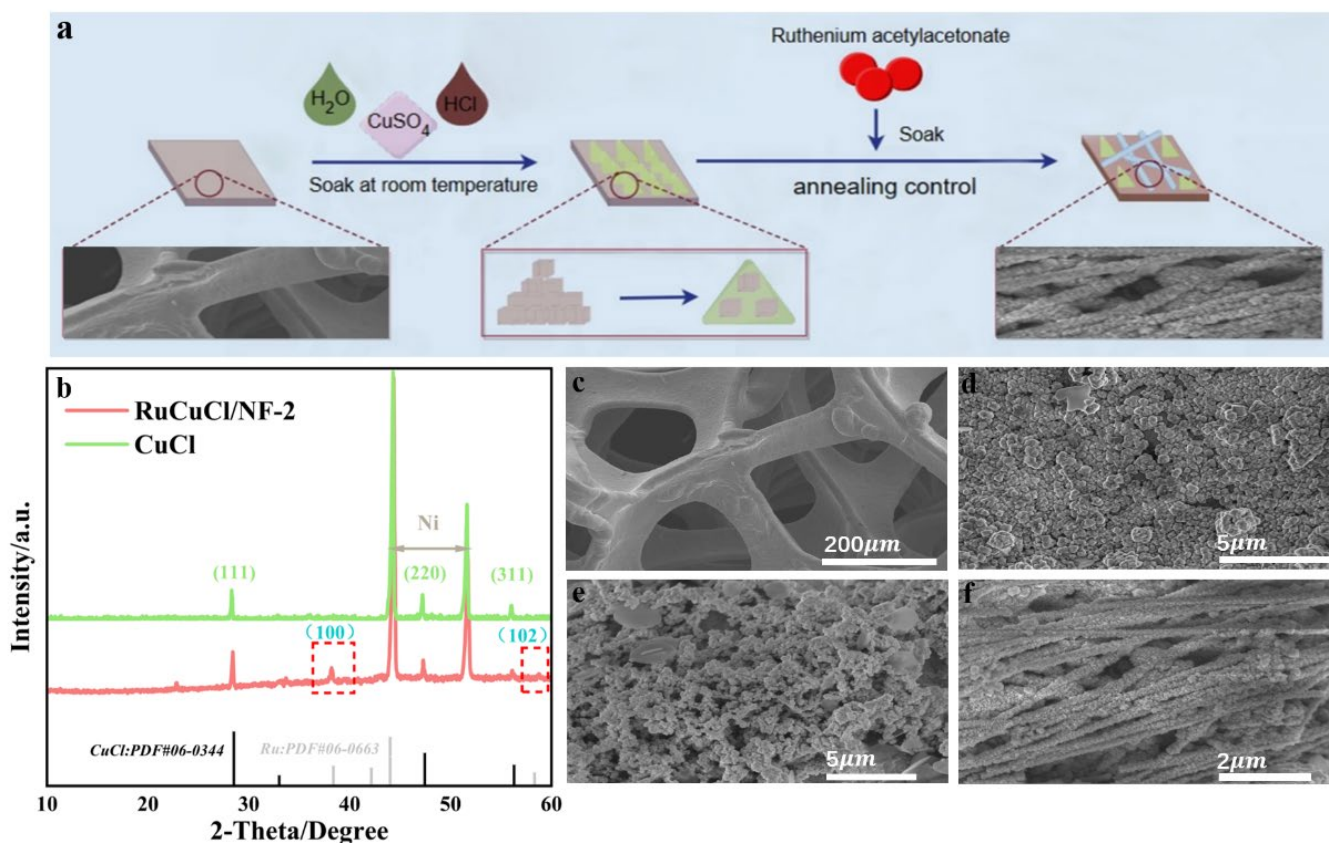


Figure 1. (a) Schematic diagram of the synthesis of a RuCuCl/NF-2 material. (b) XRD images of RuCuCl/NF-2 and CuCl/NF. (c) SEM image of NF. (d) SEM image of RuCuCl/NF-1. (e) SEM image of RuCuCl/NF-3. (f) SEM image of RuCuCl/NF-2.

Figure 1c shows the SEM image of NF, which can be seen to have a large porous skeleton structure and smooth surface. Figure S4 shows the SEM images of CuCl at different times, and it can be seen that the surface of the catalyst becomes rough after immersion treatment, and the SEM images of CuCl/NF nanostructures under different time treatments can be seen as well. The results showed that the morphology of CuCl/NF-2h depicted in Figure S4a,b showed a granular structure with germination. However, the scanned image (Figure S4c,d) of the CuCl/NF-8h sample shows that the CuCl particles self-assemble to form a conical film, which is similar to our previous expectations. Finally, the previous granular structure in CuCl/NF-12h is almost completely converted into a conical thin film structure in Figure S4e,f. This is mainly due to the redistribution and self-assembly of solid surface atoms during CuCl formation.

Generally, CuCl precursors will have different morphologies at different reaction times, but we found that it is easy to ignore one point in the preparation, that is, the effect of dissolved oxygen in the solution on the CuCl precursor during the cleaning process, and the SEM results further showed that the dissolved oxygen in the solution during the cleaning

process plays a crucial role in the morphology regulation of CuCl. As shown in Figure S5, the newly reacted CuCl precursor was soaked and cleaned only three times in deionized water for five minutes each time and then vacuum-dried and stored as a comparison sample (Figure S6), soaked and cleaned in deionized water with nitrogen exhaustion of dissolved oxygen, and the rest of the operations were consistent. We found that the morphology was more uniform, accompanied by the tendency of Cu nanoparticles to self-assemble into conical films, and in order to further verify our conjecture, we continued to conduct in-depth experiments and soaked the precursor in deionized water with nitrogen exhaustion of dissolved oxygen, which we stored in open immersion in oxygen-drained deionization (Figure S7). The SEM of the control sample is shown in Figure S8, with the main difference being that it was subsequently stored sealed. This is because the oxygen in the air will gradually dissolve in water during the process of exposure, and the SEM image results show that dissolved oxygen will have an effect on the self-assembly of Cu nanoparticles. At the 8 h reaction time, the sample morphology of the samples that were removed during early cleaning and sealed during the subsequent storage was regular, and the nanoparticles and conical films were distributed on the substrate, which was in line with our expected products, while the samples stored in the open area showed a chaotic growth trend in addition to the conical CuCl films generated during the reaction, which further indicated that the removal of dissolved oxygen from the solvent during the cleaning process had a significant effect on the morphology of the CuCl precursor.

In Figure 1d–f, the difference between RuCuCl/NF-2 and the two remaining samples is depicted. It can be seen that the presence of a special coral structure of RuCuCl/NF-2 regulates the interfacial charge distribution and promotes charge transfer at the atomic level. In addition, the retention of CuCl particles and a part of the structure, the large surface domain, significantly enhances the exposure of active sites, the collection/transport of electrons and the diffusion of protons/ions, which accelerates the electrochemical reaction kinetics and activity. In addition, its superior structural advantages effectively reduce the overpotential of electrochemical reactions, improving stability. These observations are confirmed in the analysis and discussion below.

The morphology of nanostructured materials plays an important role in their efficient performance. In order to explore the surface and interfacial topography of the obtained catalysts, the structural properties of the materials were analyzed using field emission scanning electron microscopy (SEM) techniques. First, to further validate the catalyst formation mechanism, a Ru sample (denoted Ru/NF) without a CuCl precursor was synthesized using a similar method. In addition, the eds diagram of the Ru/NF catalyst is shown in Figure S9, which is composed of Ni, Ru, and O elements. As expected, some Ru nanoclusters were also successfully loaded on the nickel foam after annealing. Comparing this phenomenon with the formation process of RuCuCl/NF-2, we found that the controlled annealing process further confirmed that the controlled annealing treatment allowed Ru to replace part of the dense CuCl substrate under the action of the CuCl precursor. As can be seen from Figure 1f, RuCuCl/NF-2 exhibits a wide range of coral-like structures. Furthermore, in the absence of CuCl precursors, almost no coral-like or other synergistic RuCuCl structures were observed, further confirming the guiding role of CuCl (Figure S10). In addition, Ru particles that were not guided by CuCl precursors were heavily agglomerated on the nickel foam substrate. Therefore, it can be seen from the above experimental results that CuCl precursors play a crucial role in the dispersion and stability of the Ru metal phase.

RuCuCl/NF-2 was placed in a tube furnace in different atmospheres for annealing and post-annealing analysis. The XRD results further revealed the content of metal Ru nanoparticles, and nitrogen gas was introduced during annealing, which significantly

reduced the loading of Ru. This is demonstrated by the missing metallic Ru diffraction peaks (Figure S11). In addition, the characteristic peaks of CuCl were observed, indicating that most of the CuCl precursors were not replaced during the annealing process, which also demonstrated the stability of CuCl as a precursor.

As shown in Figure S12, the conical CuCl precursor exposed to the NF surface is shown, indicating that the CuCl precursor also has good stability under the changes in reaction temperature, atmosphere and other environmental factors, while the missing coral structure indicates that during the annealing treatment, during the annealing process, the temperature distribution of the environment in the tube furnace may be changed when nitrogen is introduced, and the temperature change will lead to a change in the rate of the reduction reaction, which, in turn, will affect the reduction reaction of Ru elements. Therefore, the structure and morphology of the target catalyst will be changed. Figure 2a shows the eds map of CuCl, indicating the presence of Cu, Cl, O, and C elements. Figure 2c shows the eds map of RuCuCl/NF-2, indicating the presence of Ni, Cu, Cl, and Ru elements. This is mainly due to the introduction of the Ru element to replace part of the Cu element. Importantly, comparing the CuCl precursors under different preparation times, it can be clearly seen that the RuCuCl/NF-2 catalyst obtained by introducing Ru on the basis of CuCl-8h has a rough surface, a wider particle diameter and more active sites on the surface of Cu atoms, which means that CuCl-8h participates in charge transfer better in the process of proton/ion adsorption, active site exposure and electrochemical OER/HER.

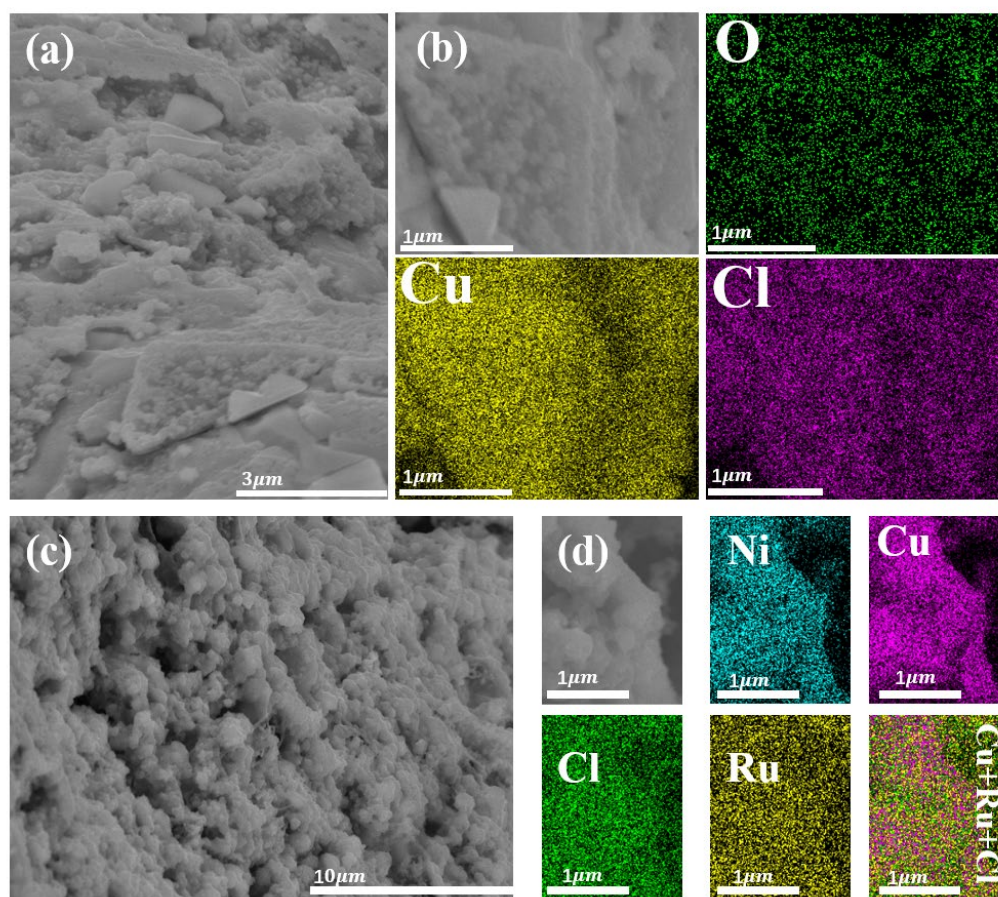


Figure 2. (a) SEM image of a CuCl-8h. (b) EDS mapping of Cu, Cl, and O elements. (c) Scanning electron microscope image of RuCuCl/NF-2. (d) EDS mapping of Cu, Cl, Ni, and Ru elements.

To elucidate the role of Ru in the Cu group, X-ray photoelectron spectroscopy (XPS) was used to trace the chemical configurations and surface electronic states of the Ru and Cu

components (Figure 3). In Figure 3a, XPS measurements of the RuCuCl/NF-2 sample show the presence of Ni, Ru, and Cu elements on the surface of the nanosheets, further indicating that Ru is successfully doped in the CuCl precursor. The Cu LMM spectra in Figure 3b,c correspond to the CuCl sample and the new Ru-doped catalyst RuCuCl/NF-2, respectively, demonstrating the presence of Cu^+ and Cu^{2+} in both catalysts. Previous studies have shown that the Cu^0 helix is about 3 eV higher than the Cu^+ helix, and, as can be seen from the Figure, the CuCl sample has only one helical peak at a binding energy of 569.1 eV, indicating that its chemical state is +1, which is CuCl [30]. There is no metallic copper on the electrodes. The lower binding energy peak in RuCuCl/NF-2 (568.8 eV) indicates that Cu exists as 2+. This is due to the inevitable occurrence of surface oxidation during the measurement of XPS, which we do not believe will affect the performance and analysis of the catalyst. In subsequent electrochemical tests, all samples are fabricated and tested on site.

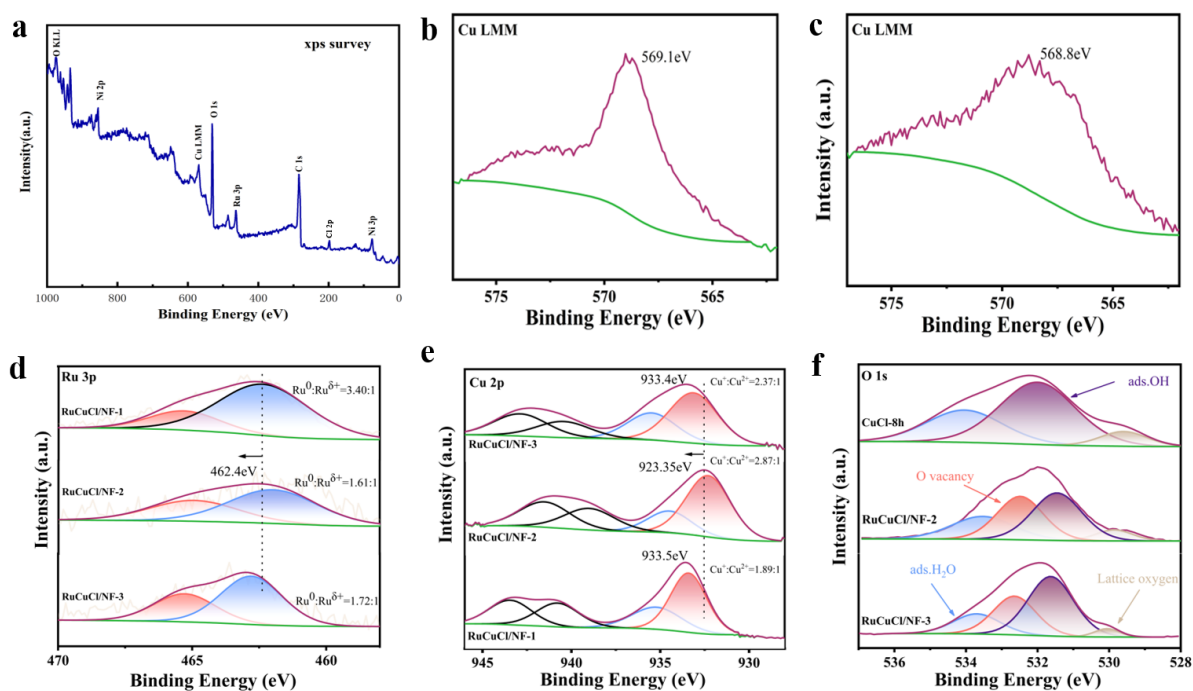


Figure 3. (a) XPS full spectrum and high-resolution XPS spectra of RuCuCl/NF-2. (b) Cu LMM of CuCl-8h. (c) Cu LMM of RuCuCl/NF-2. (d) Ru 3p. (e) Cu 2p. (f) O 1s.

Since XPS is a highly accurate characterization method, it can be inferred that the main component of RuCuCl/NF-2 is the elemental valence state rather than the oxidation state, especially in the central section, and in addition, these peaks in the figure are narrowed at the high-energy shoulder. The high-resolution XPS spectra of Ru 3p are further shown in Figure 3d. Due to the significant overlap between the Ru 3d and C1s orbitals, the Ru 3p orbital was used, instead of the Ru 3d orbital, in this study. The peak at 462.64 eV belongs to Ru 3p_{3/2}. These Ru samples consist of Ru⁰ and Ru^{δ+} states. The partial oxidation of Ru may explain the presence of Ru^{δ+}, which is due to the sensitivity of Ru and the inevitable oxidation in a high-temperature air environment during preparation and annealing. The Ru⁰/Ru^{δ+} atomic ratio was 1.61 in the RuCuCl/NF-2 sample (Figure 3d) [31].

Subsequently, by changing the precursor, the Ru⁰/Ru^{δ+} ratio increased from 1.61 to 3.40, indicating that the reaction time had a significant effect on the valence change in Ru, forming pairs of Ru-O-Cu bonds [32]. By studying the Cu 2p_{3/2} XPS spectra of RuCuCl/NF-1, RuCuCl/NF-2 and RuCuCl/NF-3, as well as the Ru 3p XPS spectra, a shift in the Ru 3p and Cu 2p_{3/2} spectra was observed. In the Ru 3p spectrum, the fitting peak 462.2 eV

corresponds to Ru^0 , and the remaining peaks belong to the $\text{Ru}^{\delta+}$ state (Figure 3d). In addition, the $\text{Cu } 2p_{3/2}$ spectrum was deconvoluted into two peaks at 932.35 eV, attributed to Cu^+ and Cu^{2+} , respectively (Figure 3e) [33]. The $\text{Cu}^+:\text{Cu}^{2+}$ ratio of RuCuCl/NF-2 is 2.87:1, which is much larger than that of other ruthenium-containing samples, indicating the existence of electron transfer from Ru to Cu [34]. The synergistic effect between Ru and Cu alters the electronic structure and surface charge redistribution of Ru, resulting in more $\text{Cu}^{0/1+}$ states, which may optimize the adsorption and bonding behavior of the active site to the reactive species. In addition, the interaction between Ru and Cu-based components allows Ru to effectively prevent the peroxidation of Cu-based components, resulting in more $\text{Cu}^{0/1+}$ species, which further justifies the previously synthesized cuprous catalyst, as an increase in the Cu^{1+} ratio can promote HER [29]. From the above results, it can be inferred that the introduction of Ru regulates the electronic structure of Cu and synergistically improves its HER performance. A comparison of the O 1s signals in Figure 3f shows the presence of a large number of oxygen vacancies on RuCuCl/NF-2. Previous studies have shown that vacancy engineering significantly enhances hydrogen evolution activity. Therefore, the vacancies and distorted lattices generated by the CuCl precursor during Ru-doped annealing are beneficial to improving the surface oxygen affinity, enhancing the effective binding to water molecules, reducing the kinetic barrier during water electrolysis and promoting the Tafel step and Volmer step, thereby improving the HER performance of RuCuCl/NF-2 under alkaline and neutral conditions, respectively, which is further verified by the O 1s XPS spectrum (Figure 3f). The peaks at 533.6, 532.5, 531.4, and 529.8 eV correspond to adsorbed water, O vacancies, OH and lattice oxygen, respectively. The RuCuCl/NF-2 catalyst has a large number of vacant O signals, indicating that there are a large number of defects on its surface [31].

2.2. Electrochemical Characterization

In order to further explore the behavior of the designed unique nanomaterials, the electrocatalytic activity of the prepared NF, CuCl/NF, Ru/NF, Pt/NF, RuCuCl/NF-2, and RuCuCl/NF-2 on a universal three-electrode platform was analyzed in a 1.0 M KOH alkaline medium with a scan rate of 5 mV s^{-1} . Figure 4a shows the linear sweep voltammetry (LSV) curves of the obtained samples in the case of IR compensation to show their electrochemical activity. In contrast, the overpotentials of the composite RuCuCl/NF-2 coral structure was 25 and 70 mV at current densities of 10 and 50 mA cm^{-2} , respectively, showing the best electrocatalytic activity. It was significantly lower than NF (231 and 340 mV at 10 and 50 mA cm^{-2}), CuCl/NF (112 and 259 mV at 10 and 50 mA cm^{-2}), Ru/NF (49 and 195 mV at 10 and 50 mA cm^{-2}) and Pt/NF (38 and 83 mV at 10 and 50 mA cm^{-2} , respectively) [9].

Then, to reveal the electrochemical reaction kinetics of the resulting sample, we calculated the Tafel slope corresponding to LSV in Figure 4a. As shown in Figure 4c, the Tafel slope of RuCuCl/NF-2 is 21.9 mV dec^{-1} , which is much lower than that of NF (364 mV dec^{-1}), Ru/NF (117 mV dec^{-1}), CuCl/NF (220 mV dec^{-1}) and Pt/NF (32.9 mV dec^{-1}). The lower Tafel slope indicates that the hydrogen evolution reaction (HER) for the RuCuCl/NF-2 catalyst follows the Volmer–Tafel mechanism, with the Tafel step serving as the rate-determining step (RDS). In this mechanism, the first step involves the adsorption of protons (H^+) onto the catalyst surface, forming an adsorbed hydrogen atom (H^*), which constitutes the Volmer step. The subsequent step involves the combination of two adsorbed hydrogen atoms to form molecular hydrogen (H_2), known as the Tafel step. Since the Tafel step is slower and more energy-intensive than the Volmer step, it becomes the rate-limiting step in the overall reaction. The observed low Tafel slope for RuCuCl/NF-2 suggests that the catalyst effectively facilitates this rate-limiting Tafel step, thereby enhancing the

overall performance of the hydrogen evolution reaction [35,36]. The results above suggest that the unique coral-like morphology, along with the regulation of complex interfacial charge distribution and the facilitation of atomic-level charge transfer within the catalyst, can significantly accelerate electron transfer and enhance the exposure of active electrons, ultimately improving the kinetics of electrochemical reactions. The results indicate that Ru has a significant activating effect on the hydrogen production ability of Cu-based catalysts, and that RuCu exhibits a synergistic enhancement in the hydrogen production performance of the catalyst. In addition, the long-term electrocatalytic durability of the electrode material is another key factor in evaluating the superiority of the catalyst. Figure 4e shows the comparison of the LSV curves of RuCuCl/NF-2 after a durability test, and there is no obvious attenuation compared with the initial state, which, once again, proves its excellent stability. At the initial current density of 20mA cm^{-2} , the reaction time of more than 100 h still maintains good stability [37].

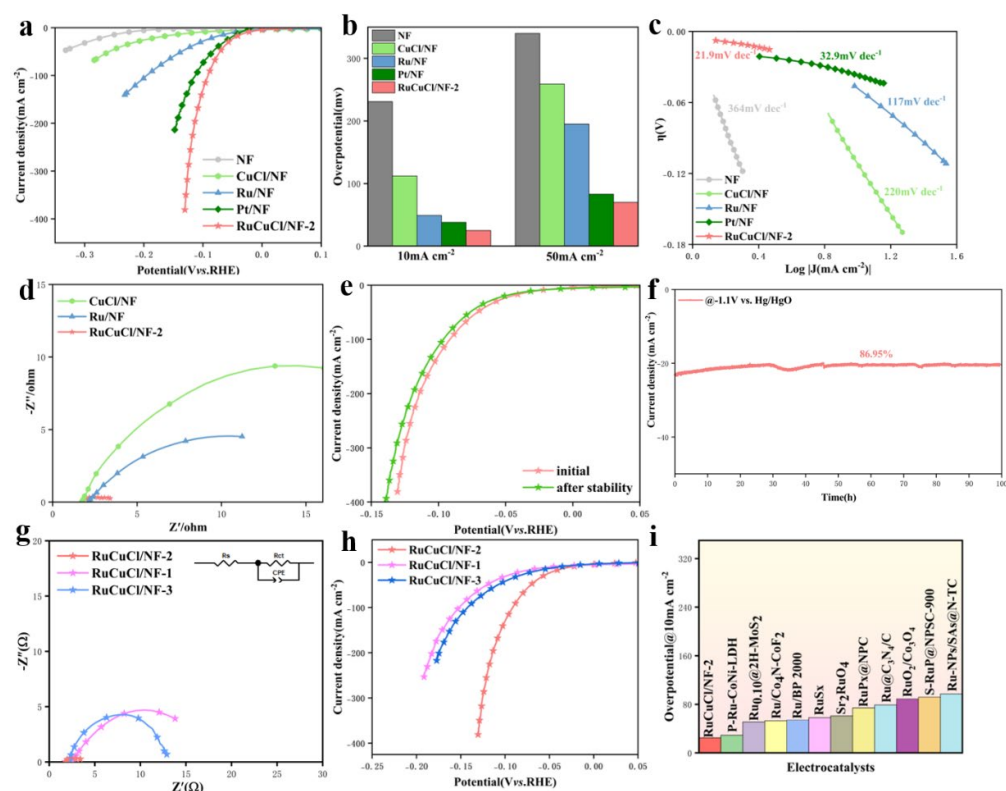


Figure 4. Comparison of HER performance of NF, CuCl/NF, Ru/NF, Pt/NF and RuCuCl/NF-2 samples: (a) LSV polarization curves; (b) overpotentials at 10, 50 mA cm^{-2} ; (c) Tafel plots; (d) Nyquist plots of CuCl/NF, Ru/NF and RuCuCl/NF-2 samples; (e) comparison of LSV curves before and after stability tests; (f) i-t curves; (g) Nyquist plots of RuCuCl/NF-1, RuCuCl/NF-2 and RuCuCl/NF-3 samples; (h) RuCuCl/NF-1, RuCuCl/NF-2 and LSV polarization curves of RuCuCl/NF-3 samples; and (i) η_{10} of RuCuCl/NF-2 in comparison with already reported Ru-based catalysts.

Remarkably, in Figure 4f,h, it is found that the performance gap widens significantly after changing the reaction time of the CuCl precursor to 2 h and 12 h. This is usually due to the larger size of the metal system, less exposure to the electrolyte, high electron density and generally slow water adsorption and dissociation kinetics, as well as limited metal substrate synergy, such as the negative shift in the polarization curve towards a higher potential and the increase in the Tafel impedance value [38]. These results indicated that the CuCl precursor under the composite morphology of particles and cones had a significant promoting effect on the subsequent catalytic activity of RuCuCl/NF-2. In addition, an electrochemical impedance spectroscopy (EIS) showed that RuCuCl/NF-2 exhibited the

lowest Rct of about 2.5Ω , indicating that the electron transfer was easy and rapid. In addition, RuCuCl/NF-2 shows an overpotential value of only 25 mV at 10 mA cm^{-2} , which is significantly better than other reported ruthenium-based catalysts (Figure 4i). The above experimental and measurement results show that RuCuCl/NF-2 has the most significant electrochemical activity and stability medium in the alkaline environment [39,40].

Typically, the catalytic activity of a catalyst is intimately tied to its electrochemical surface area (ECSA) [41]. To accurately determine the intrinsic activity of different RuCu electrocatalysts and assess the active sites on the catalyst surface, we tested the current density variation in the three catalysts at different scan rates in a 1 M KOH electrolyte. The CV curves of all three catalysts exhibited relatively regular rectangular shapes. Additionally, we plotted the current density at the average potential of each catalyst against the corresponding scan rate, with the relationship between scan rate and current density shown in Figure 5. Since ECSA is linearly proportional to the double-layer capacitance (Cdl), we calculated the Cdl for each catalyst using cyclic voltammetry (CV), resulting in the following order: RuCuCl/NF-2 (74.9 mF cm^{-2}) > RuCuCl/NF-2 (38.5 mF cm^{-2}) > RuCuCl/NF-1 (31.8 mF cm^{-2}). A larger Cdl value indicates a higher ECSA, suggesting that more active sites are exposed, which contributes to the enhanced electrocatalytic performance (Figure 5d). These electrochemical results confirm that the designed and synthesized RuCu catalysts, with their synergistic effects, have a larger electrochemical surface area and more active sites, which likely contribute to the superior catalytic performance of the RuCuCl/NF-2 electrocatalyst [42].

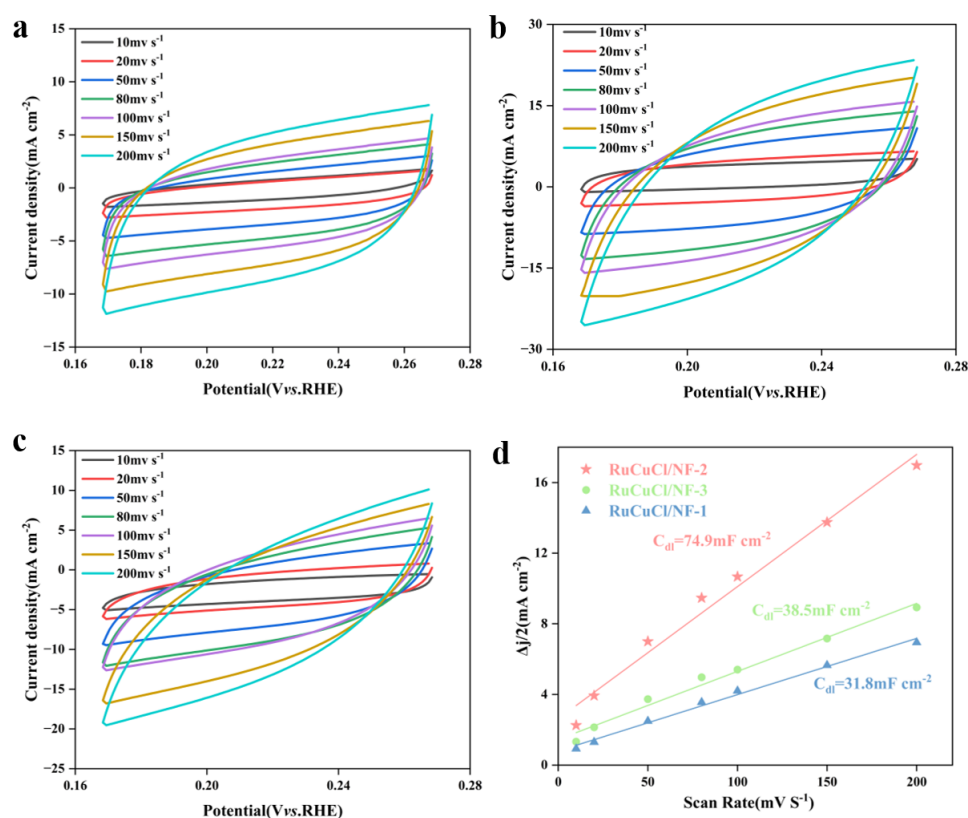


Figure 5. The CV curves of (a) RuCuCl/NF-2, (b) RuCuCl/NF-2 and (c) RuCuCl/NF-2 with different scanning rates of $10 \text{ mV} \cdot \text{s}^{-1}$, $20 \text{ mV} \cdot \text{s}^{-1}$, $50 \text{ mV} \cdot \text{s}^{-1}$, $80 \text{ mV} \cdot \text{s}^{-1}$, $100 \text{ mV} \cdot \text{s}^{-1}$, $150 \text{ mV} \cdot \text{s}^{-1}$ and $200 \text{ mV} \cdot \text{s}^{-1}$ towards HER. (d) Comparison of Cdl values of each catalyst.

The electrochemical OER properties of NF, CuCl/NF, Ru/NF, and RuCuCl/NF-2 were characterized for the first time on a standard three-electrode platform at 1.0 M KOH and 5 mV s^{-1} . Figure 6a shows the linear swept voltammetry (LSV) curve of the catalyst after

IR compensation. Compared with NF, CuCl/NF and Ru/NF, RuCuCl/NF-2 exhibited the best OER electrocatalytic activity [43].

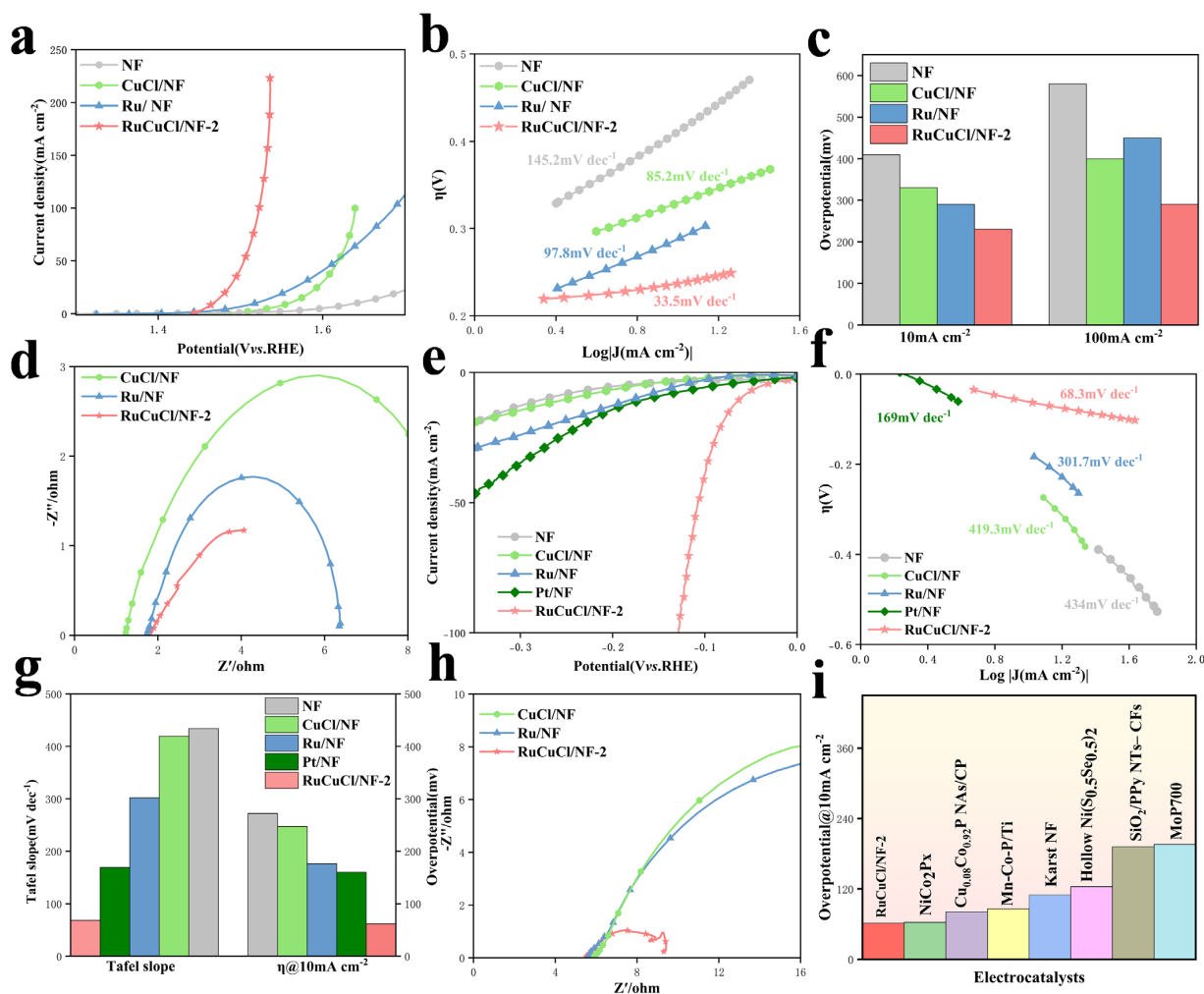


Figure 6. Comparison of OER performance of NF, CuCl/NF, Ru/NF, and RuCuCl/NF-2 samples at 1 M KOH: (a) LSV polarization curves; (b) Tafel plots; (c) overpotentials at 10, 50 mA cm⁻²; (d) Nyquist plots for CuCl/NF, Ru/NF, RuCuCl/NF-2 samples; (e) HER polarization curves of NF, CuCl/NF, Ru/NF, Pt/NF and RuCuCl/NF-2 samples under 1 M PBS; (f) Tafel plots; (g) Tafel and overpotential at 10 mA cm⁻²; (h) Nyquist plots of CuCl/NF, Ru/NF, RuCuCl/NF-2 samples; and (i) comparison of η_{10} of RuCuCl/NF-2 with already reported Ru-based catalysts.

Figure 6b shows the resulting Tafel slopes for NF (145.2 mV dec⁻¹), CuCl/NF (85.2 mV dec⁻¹), Ru/NF (97.8 mV dec⁻¹) and RuCuCl/NF-2 (33.5 mV dec⁻¹). These results further indicate that RuCuCl/NF-2 synthesized by the controlled annealing process has unique physicochemical properties, which can effectively accelerate the catalytic rate and electrochemical kinetics, and the presence of a unique coral-like structure significantly exposes more active sites and accelerates OER activity [44]. Figure 6c shows a comparison of the overpotentials of CuCl/NF, NF, Ru/NF, and RuCuCl/NF-2 at 10 and 100 mA cm⁻², with the smallest overpotential for RuCuCl/NF-2. The overpotential of RuCuCl/NF-2 at 10 mA cm⁻² is 230 mV, which is much lower than that of NF (410 mV), CuCl/NF (330 mV) and Ru/NF (290 mV). These results show that the synergistic effect between the constructed Ru and CuCl precursors fundamentally promotes the transfer of active electrons and the exposure of active centers and significantly improves the OER activity of the electrocatalyst. To gain a deeper understanding of the OER kinetics of the RuCuCl/NF-2 catalyst, the

electrochemical impedance spectroscopy (EIS) was measured. We collected Nyquist plots to determine the charge transfer resistance (R_{ct}), which is generally considered to be a valid descriptor of catalytic reaction kinetics, and as shown in Figure 6d, the impedance values of RuCuCl/NF-2 are significantly lower than those of CuCl/NF and Ru/NF. The results showed that the charge transfer kinetics of the RuCuCl/NF-2 catalyst were the fastest among the three samples under the same conditions.

Notably, the obtained target catalyst was tested for OER/HER in 1 M PBS, which further verified its significant electrochemical activity in neutral media, as shown in Figure 6e–h. The linear swept voltammetry curves of CuCl/NF, Ru/NF, Pt/NF, RuCuCl/NF-2 and HER on IR compensation can be observed. Among them, the overpotential of the target RuCuCl/NF-2 catalyst is 81.9 mV and 128 mV at current densities of 50 and 100 mA cm⁻², respectively, and the comparison of Tafel slopes and electrochemical impedance also highlights that RuCuCl/NF-2 has the best HER performance. Finally, RuCuCl/NF-2 still exhibits excellent HER activity in neutral media compared to most of the reported HER catalysts (Figure 6i). Then, the electrocatalytic OER activity of the samples was determined under 1 M PBS conditions. As shown in Figure S13, RuCuCl/NF-2 has the best catalytic activity among all samples because it produces the highest current density (J) at the same overpotential (η). For a better comparison, we also researched the OER performance of pure nickel foam, of which the effect of nickel foam on OER performance through structural evolution is negligible (Figure S13). We also predict the OER kinetics of the electrocatalyst by plotting the overpotential versus logarithm (J). As expected, RuCuCl/NF-2 has the lowest Tafel slope (86.5 mV dec⁻¹), and to reveal the electron transport dynamics, EIS measurements were also performed (Figure S13d). Similarly to the OER case under the alkaline conditions discussed earlier, RuCuCl/NF-2 has the smallest R_{ct} value. These results indicate that RuCuCl/NF-2 is the most favorable for the reaction kinetics of OER.

The exceptional OER and HER capabilities led to its use in evaluating the overall water splitting (OWS) performance, as schematically depicted in Figure 7a. As shown in Figure 7b, the RuCuCl/NF-2 || RuCuCl/NF-2 configuration demonstrates remarkable efficiency, requiring significantly lower voltages of 1.489 V and 1.585 V to reach current densities of 10 and 20 mA cm⁻², respectively. Furthermore, as clearly shown in Figure 7c, the RuCuCl/NF-2 electrode demonstrated sustained operation at a constant overpotential for over 10 h in an alkaline solution, maintaining a stable current density. This further underscores the stability of the RuCuCl/NF-2 catalyst material [45].

As displayed in Figure 7d (Table S3), when compared with reported bifunctional HER/OER electrocatalysts for water splitting, this catalyst exhibits an outstanding performance, highlighting its promising potential for water splitting applications.

The aforementioned information indicates that the first step in the creation of extremely active RuCu catalysts is the CuCl precursor treatment. We postulated that ruthenium–copper coral-like nanorods are generated by a coordination interaction between CuCl precursors and ruthenium ions in order to gain a better understanding of the changes in the catalytic process (Figure 6b). Granular CuCl generates vacancies on the nickel foam's surface and disperses Ru atoms during the development process, but the self-assembled conical CuCl successfully retains Ru atoms.

Additionally, during the Ru doping process, Cl⁻ ions can coordinate with metal sites to balance the charge within the catalyst. This phenomenon has been confirmed by a Cl 2p XPS analysis (Figure 8a).

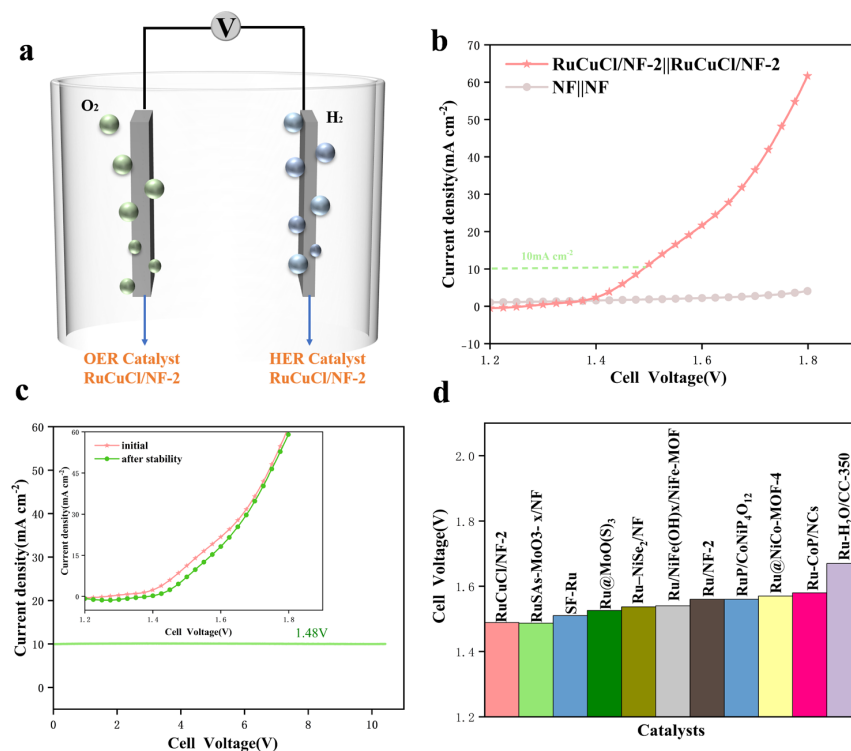


Figure 7. (a) Schematic diagram of RuCuCl/NF-2 as anode and cathode for OWS. (b) LSV curves of catalyst. (c) Chronoamperometry curve of RuCuCl/NF-2 || RuCuCl/NF-2 toward overall water splitting. (d) Comparison of RuCuCl/NF-2 with recently reported Ru-doped catalysts for overall water splitting.

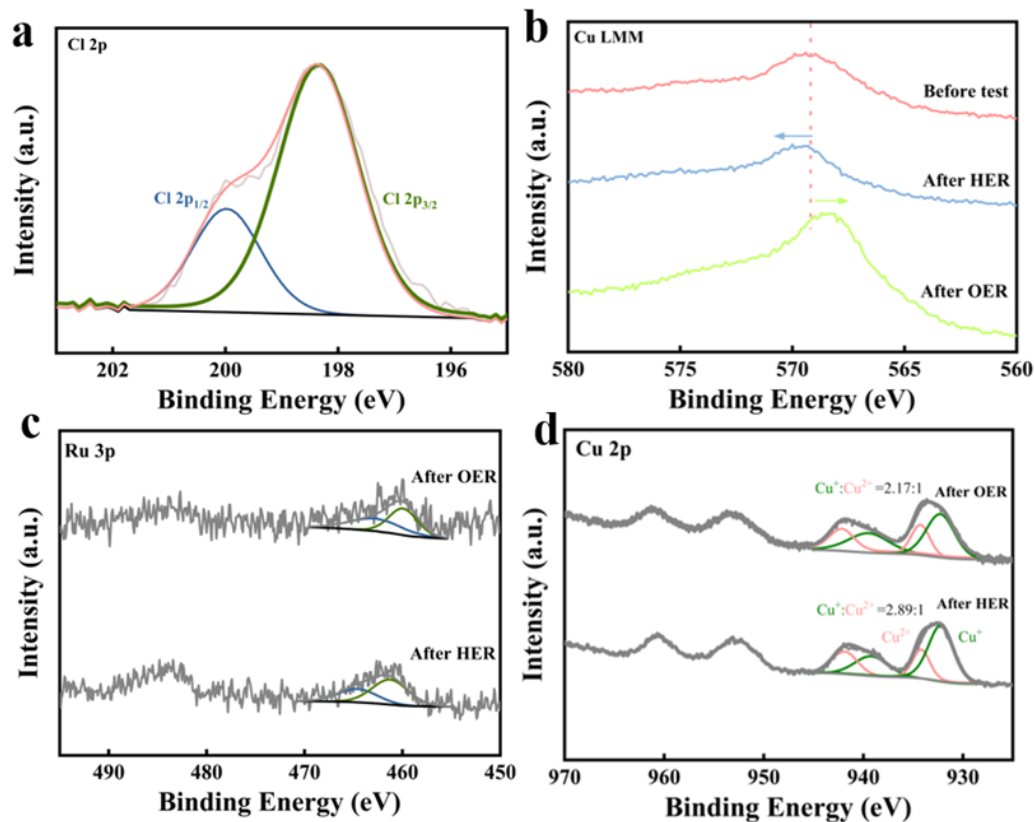


Figure 8. (a) High-resolution XPS spectra of Cl 2p of RuCuCl/NF-2. High-resolution XPS spectra of Cu LMM (b), Ru 3p (c), and Cu 2p (d) for RuCuCl/NF-2 after the OER and HER.

An XPS further analyzed the chemical environment changes during water electrolysis. As shown in Figure 8b,d, the Cu 2p_{3/2} XPS spectra confirmed that the introduction of Ru enhances the catalyst's electronic conductivity and electrocatalytic activity, facilitating electron transfer at the catalyst surface and maintaining the stability of Cu⁺. These results indicate that the structure and composition of RuCuCl/NF-2 underwent relatively minor changes during water electrolysis tests and further confirmed that the enhanced stability is attributed to the synergistic regulation between Ru and Cu [46].

As illustrated in Figure 8c, the characteristic peaks of Ru⁰ and Ru^{δ+} are still identifiable in the corresponding HER and OER spectra. The zero-valent Ru remains intact, although the proportion of Ru oxides slightly increases during OER, likely due to the frequent redox reactions occurring in the electrocatalytic process [47].

To facilitate the deposition of Ru atoms on nickel foam and to aid in the successful fabrication of ruthenium-copper coral-like nanorods, CuCl successfully adsorbed to all of the surfaces of the nickel foam. It can be seen from an SEM (Figure S4d) that, under the capture and guidance of the two forms of CuCl, more active sites were retained, which promoted the formation of regular chain coral structure in RuCuCl/NF-2 samples and enhanced the water electrolysis capacity of RuCuCl/NF-2. RuCuCl/NF-1 (Figure 9a) and RuCuCl/NF-2 (Figure 9b) share the same growth mechanism. The granular CuCl precursor sticks to the nickel foam's surface, but the conical CuCl that is missing is unable to capture enough Ru atoms, forming morphologies like those shown in (Figure 9a). A diagram of the scattered RuCu particle structure is presented. On the other hand, the CuCl-12h sample had a fully formed conical thin-film structure and could efficiently extract Ru atoms to produce ruthenium nanoparticles. However, as seen in its SEM image (Figure S4f), the agglomeration of Ru atoms is due to the inadequate allocation of the RuCu structure due to the absence of granular CuCl precursors, which is why its HER performance is in the middle (Figure 9c).

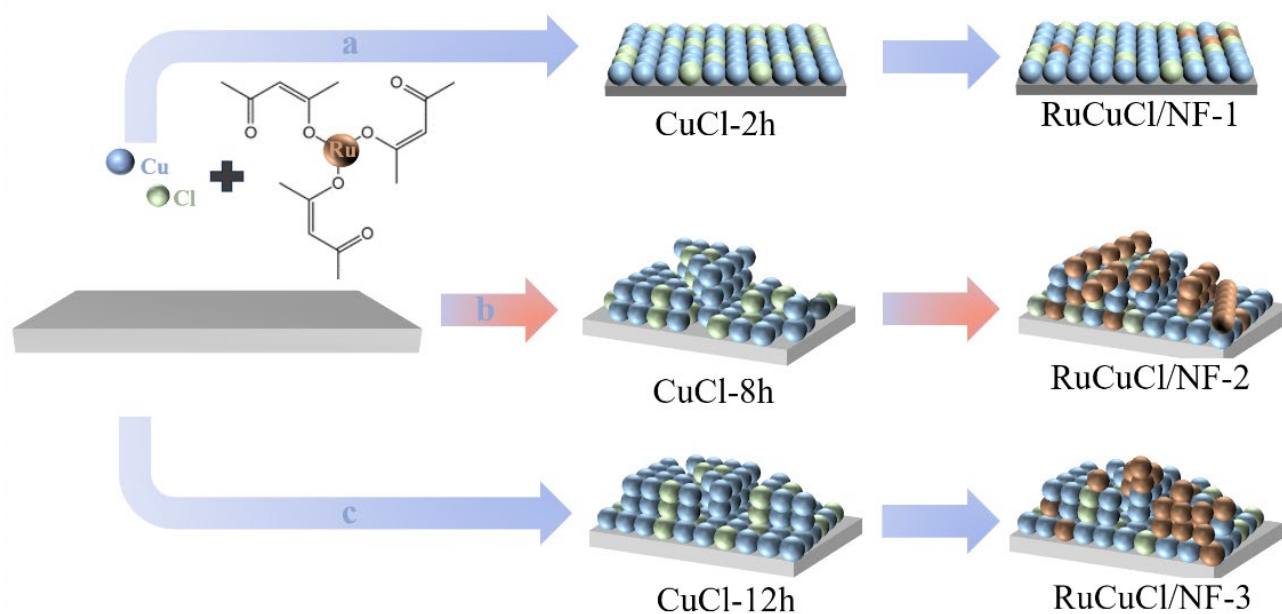


Figure 9. Schematic diagram for the regulation of Cu-based constituents: (a) CuCl-2h, RuCuCl/NF-1; (b) CuCl-8h, RuCuCl/NF-2; and (c) CuCl-12h, RuCuCl/NF-3.

3. Materials and Methods

3.1. Materials

The materials used include ruthenium acetylacetonate, copper sulphate pentahydrate (purchased from Shanghai McLean Company, Shanghai, China), nickel foam (1 cm × 2 cm),

hydrochloric acid (analytically pure) and deionized water. All reagents were used directly without further purification.

3.2. Treatment of Nickel Foam

The nickel foam was cut into 1 cm × 2 cm rectangles and washed with 1 M hydrochloric acid, acetone, deionized water and alcohol for 10 min before use, then dried under vacuum at 50 °C for 5 h. It was then sealed and set aside.

3.3. Configuration of Reaction Solution

Convert 0.25g CuSO₄ into a 40 mL solution, perform magnetic stirring for 30 min, then add 150 µL HCl. Seal and set it aside after stirring for another 30 min.

3.4. Synthesis of Electrocatalysts

3.4.1. Synthesis of CuCl-2h, CuCl-8h, CuCl-12h

Place the pre-treated fresh nickel foam sheets into a number of 7 mL centrifuge tubes, add the configured copper sulfate solution, and place the nickel foam with the same angle of tilt each time. Set the immersion time to 2 h, 8 h and 12 h. After the reaction, rinse the obtained compounds with deionized water, blow dry with nitrogen, then them in a vacuum desiccator for storage at room temperature.

3.4.2. Synthesis of RuCuCl/NF-2

Dissolve an appropriate amount of ruthenium acetylacetonate solution in isopropanol and convert it into a supersaturated solution. Soak the CuCl-8h sample in a beaker with the supernatant for 2 h. After 2 h, remove the sample and blow dry with nitrogen. Place the above samples in a tube furnace for annealing, setting the temperature to 300 degrees. Increase the temperature by 5 °C/min for 90 min, with the atmosphere conditions as follows: no ventilation and annealing in air.

3.4.3. Synthesis of RuCuCl/NF-1, RuCuCl/NF-3

For the preparation of the other RuCuCl catalysts, the process was the same as for RuCuCl/NF-2, except that RuCuCl/NF-1 and RuCuCl/NF-3 were immersed in CuSO₄/HCl solution for 2 h and 12 h.

3.4.4. Synthesis of Pt/NF

For the preparation of the Pt/NF catalyst, the mass change from NF to RuCuCl/NF-2 was measured for the preparation of RuCuCl/NF-2, which were 0.0005 g, 0.0013 g and 0.0008 g, respectively, to obtain the average mass of loaded Ru as 0.0008 g, and the loading versus area was obtained to be 0.4 mg/cm².

Pt/NF electrodes are synthesized by a coating method previously reported elsewhere. To prepare the electrode, commercially available Pt/C powder and Nafion's ethanol solution were dispersed in a mixture solution containing H₂O and ethanol. Pt/C ink was dropped onto pretreated NF with an area of 0.5 cm² and dried under infrared light.

3.5. Characterization

Scanning electron microscope (SEM, Hitachi Regulus 8220, Hitachi, Tokyo, Japan) images were used for the structural characterization of the prepared samples. X-ray diffraction (XRD, Panalytical Pyrean, Malvern Panalytical, Malvern, UK) patterns for crystal structure and phase analysis were characterized using Cu K α radiation, with a scanning range typically from 10° to 80° and a scanning speed of 4°/min. X-ray photoelectron spectroscopy (XPS, ESCALAB 250Xi, Thermo Fisher Scientific, Waltham, MA, USA) was

used to analyze the elemental compositions, chemical states, and molecular structures in order to determine the composition of the materials and the bonding states of the elements.

3.6. Electrochemical Measurement

On an electrochemical workstation (Chi760e, CH Instruments, Bee Cave, TX, USA), a Hg/HgO electrode was used as the reference electrode, a graphite rod as the counter electrode, and the prepared sample electrode as the working electrode in an alkaline environment. Specifically, the prepared nickel foam catalyst (1 cm × 0.5 cm) was used as the working electrode, 1.0 M KOH aqueous solution was used as the electrolyte, and the HER and OER of the catalyst were measured after cleaned with pure Ar. The relationship between the reference potential and the potential of the reversible hydrogen electrode was $E(\text{RHE}) = E(\text{Hg}/\text{HgO}) + 0.098 + 0.059 \times \text{pH}$, where $E(\text{RHE})$ is the reference potential and $E(\text{Hg}/\text{HgO})$ is the measured potential of the reference electrode for Hg/HgO, and all potential values in this study are based on the corrected reversible hydrogen electrode (RHE) values. In addition, a 1.0 M PBS solution (with Ag/AgCl electrode as the reference electrode) was used to evaluate its performance in a neutral electrolyte, and the potentials of HER and OER were calculated based on the reversible hydrogen electrode (RHE) with the formula: $E(\text{RHE}) = E(\text{Ag}/\text{AgCl}) + 0.197 + 0.059 \times \text{PH}$. The reaction areas were all set to 0.5 cm² by extending the LSV curves, and the Tafel slope was calculated by plotting the overpotential versus log (current density). EIS measurements were performed at a range of potentials. The frequency range was from 100 KHz to 0.01 Hz and the applied voltage amplitude was 5 mV. The EIS results were fitted using ZsimpWin 3.60 software.

4. Conclusions

In summary, the RuCu synergistic approach can be easily used to manufacture the highly active RuCuCl/NF-2 electrocatalyst. In our system, Ru partially displaces the Cu site to improve the creation of coral structures, and CuCl precursors act as stabilizing and guiding agents to facilitate the formation of efficient catalysts. According to experimental findings, the electrical structure of the Cu phase is enhanced by adding an appropriate amount of Ru, which induces more oxygen vacancies and increases the ratio of Cu^{0/1+}. The formation of Cu^{0/1+} states is aided by the interaction between Ru and Cu. Hydrogen production is encouraged by the interaction between Ru and the Cu¹⁺-dominated configuration. The generated RuCuCl/NF-2 has good HER performance, as predicted, with quick reaction kinetics, high activity and stability, especially in alkaline electrolytes. This suggests that it has the potential to be used in a range of industrial settings under alkaline circumstances.

Supplementary Materials: The following supporting information can be downloaded at: <https://www.mdpi.com/article/10.3390/catal15010098/s1>, Figure S1. XRD spectrum of NF SEM. Figure S2. XRD spectra of CuCl-2h, CuCl-8h, and CuCl-12h. Figure S3. XRD spectra of RuCuCl/NF-1, RuCuCl/NF-2, and RuCuCl/NF-3. Figure S4. (a,b) SEM images of CuCl-2h. (c,d) SEM images of CuCl-8h. (e,f) CuCl-12h. Figure S5. (a,b) SEM CuCl samples were washed by immersion in deionized water for 5 min three times after completion of the reaction and stored in vacuum drying. Figure S6. (a–d) SEM CuCl samples were washed after completion of the reaction by immersion in deionized water with dissolved oxygen exhausted by nitrogen for 5 min three times, vacuum dried and stored for backup. Figure S7. (a–d) SEM CuCl samples were cleaned after completion of the reaction by immersion in deionized water drained of dissolved oxygen by nitrogen for 5 min three times, after which they were placed in deionized drained of oxygen and sealed for storage. Figure S8. (a–d) SEM CuCl samples were removed from the NF after completion of the reaction and washed by immersion in deionized water with dissolved oxygen exhausted by nitrogen for 5 min three times, after which it was placed in deionized with oxygen exhausted and stored open. Figure S9. SEM images of Ru/NF

and eds mapping profiles of Ni, Ru, and O elements. Figure S10. (a) SEM image of RuCuCl/NF-2. (b) TEM image of RuCuCl/NF-2. Figure S11. XRD spectra of RuCuCl/NF-2-N₂. Figure S12. (a,b) SEM RuCuCl/NF-2-N₂. Figure S13. Evaluation and comparison of OER performance of NF, CuCl/NF, Ru/NF, and RuCuCl/NF-2 electrodes in neutral environment: (a) Polarization curves. (b) Tafel plots. (c) Overpotential at current density of 10 mA/cm², and tafel slope comparison. (d) Nyquist plots. Table S1. Comparison of the HER performance of RuCuCl/NF-2 catalysts under neutral conditions with recently reported electrolyzed water catalysts. Table S2. comparison of the HER performance of RuCuCl/NF-2 with recently reported Ru-based catalysts. Table S3. Comparison of RuCuCl/NF-2 with recently reported Ru-doped catalysts for overall water splitting. Refs. [48–74] are cited in the Supplementary Materials.

Author Contributions: T.C.: writing—original draft, software, investigation, data curation, validation. X.K.: writing—review and editing, supervision. Q.L.: writing—review and editing, supervision, project administration, methodology, investigation. All authors have read and agreed to the published version of the manuscript.

Funding: This research was funded by the Natural Science Fund for Colleges and Universities in Anhui Province, grant number 2022AH030057.

Data Availability Statement: The data will be made available upon request.

Conflicts of Interest: The authors declare that there are no conflicts of interest.

Abbreviations

HER	Hydrogen evolution reaction
OER	Oxygen evolution reaction
EIS	Electrochemical impedance spectroscopy
XRD	X-ray diffraction
SEM	Scanning electron microscopy
EDS	Energy-dispersive X-ray spectroscopy
XPS	X-ray photoelectron spectroscopy

References

1. Seh, Z.W.; Kibsgaard, J.; Dickens, C.F.; Chorkendorff, I.B.; Nørskov, J.K.; Jaramillo, T.F. Combining theory and experiment in electrocatalysis: Insights into materials design. *Science* **2017**, *355*, eaad4998. [[CrossRef](#)] [[PubMed](#)]
2. He, L.-G.; Cheng, P.-Y.; Cheng, C.-C.; Huang, C.-L.; Hsieh, C.-T.; Lu, S.-Y. (Ni_xFeyCo_{6-x-y})Mo₆C cuboids as outstanding bifunctional electrocatalysts for overall water splitting. *Appl. Catal. B Environ.* **2021**, *290*, 120049. [[CrossRef](#)]
3. Li, C.; Jang, H.; Kim, M.G.; Hou, L.; Liu, X.; Cho, J. Ru-incorporated oxygen-vacancy-enriched MoO₂ electrocatalysts for hydrogen evolution reaction. *Appl. Catal. B Environ. Energy* **2022**, *307*, 121204. [[CrossRef](#)]
4. Chen, Q.; Nie, Y.; Ming, M.; Fan, G.; Zhang, Y.; Hu, J.-S. Sustainable synthesis of supported metal nanocatalysts for electrochemical hydrogen evolution. *Chin. J. Catal.* **2020**, *41*, 1791. [[CrossRef](#)]
5. Han, C.; Mei, B.; Zhang, Q.; Zhang, H.; Yao, P.; Song, P.; Gong, X.; Cui, P.; Jiang, Z.; Gu, L.; et al. Atomic Ru coordinated by channel ammonia in V-doped tungsten bronze for highly efficient hydrogen-evolution reaction. *Chin. J. Catal.* **2023**, *51*, 80. [[CrossRef](#)]
6. Ren, X.; Zhai, Y.; Yang, N.; Wang, B.; Liu, S. Lattice Oxygen Redox Mechanisms in the Alkaline Oxygen Evolution Reaction. *Adv. Funct. Mater.* **2024**, *34*, 2401610. [[CrossRef](#)]
7. Zhang, Y.; Hui, Z.X.; Zhou, H.Y.; Zai, S.F.; Wen, Z.; Li, J.C.; Yang, C.C.; Jiang, Q. Ga doping enables superior alkaline hydrogen evolution reaction performances of CoP. *Chem. Eng. J.* **2022**, *429*, 132012. [[CrossRef](#)]
8. Gultom, N.S.; Abdullah, H.; Hsu, C.N.; Kuo, D.H. Activating nickel iron layer double hydroxide for alkaline hydrogen evolution reaction and overall water splitting by electrodepositing nickel hydroxide. *Chem. Eng. J.* **2021**, *419*, 129608. [[CrossRef](#)]
9. Li, L.; Sun, H.; Xu, X.; Humayun, M.; Ao, X.; Yuen, M.F.; Xue, X.; Wu, Y.; Yang, Y.; Wang, C. Engineering Amorphous/Crystalline Rod-like Core–Shell Electrocatalysts for Overall Water Splitting. *ACS Appl. Mater. Interfaces* **2022**, *14*, 50783. [[CrossRef](#)]
10. Ju, H.; Badwal, S.; Giddey, S. A comprehensive review of carbon and hydrocarbon assisted water electrolysis for hydrogen production. *Appl. Energy* **2018**, *231*, 502. [[CrossRef](#)]
11. Li, L.; Qiu, H.; Zhu, Y.; Chen, G.; She, S.; Guo, X.; Li, H.; Liu, T.; Lin, Z.; Zhou, H.; et al. Atomic ruthenium modification of nickel-cobalt alloy for enhanced alkaline hydrogen evolution. *Appl. Catal. B Environ.* **2023**, *331*, 122710. [[CrossRef](#)]

12. Ni, W.; Krammer, A.; Hsu, C.-S.; Chen, H.M.; Schüler, A.; Hu, X. Ni₃N as an Active Hydrogen Oxidation Reaction Catalyst in Alkaline Medium. *Angew. Chem. Int. Ed.* **2019**, *58*, 7445. [[CrossRef](#)] [[PubMed](#)]
13. Gultom, N.S.; Li, C.H.; Kuo, D.H.; Silitonga, M.Z. Multiphase Fe-doped Ni₃S₂/MoOx electrocatalyst prepared by facile one-step hydrothermal for full-cell water splitting: Effect of Mo on physical and electrochemical properties. *Appl. Catal. B Environ. Energy* **2024**, *353*, 124100. [[CrossRef](#)]
14. An, L.; Yang, F.; Fu, C.; Cai, X.; Shen, S.; Xia, G.; Li, J.; Du, Y.; Luo, L.; Zhang, J. A Functionally Stable RuMn Electrocatalyst for Oxygen Evolution Reaction in Acid. *Adv. Funct. Mater.* **2022**, *32*, 2200131. [[CrossRef](#)]
15. Chen, J.; Chen, C.; Chen, Y.; Wang, H.; Mao, S.; Wang, Y. Improving alkaline hydrogen evolution reaction kinetics on molybdenum carbide: Introducing Ru dopant. *J. Catal.* **2020**, *392*, 313. [[CrossRef](#)]
16. Zhang, L.; Xiong, K.; Chen, S.; Li, L.; Deng, Z.; Wei, Z. In situ growth of ruthenium oxide-nickel oxide nanorod arrays on nickel foam as a binder-free integrated cathode for hydrogen evolution. *J. Power Sources* **2015**, *274*, 114. [[CrossRef](#)]
17. Liu, N.; Zhai, Z.; Yu, B.; Yang, W.; Cheng, G.; Zhang, Z. Bifunctional nanoporous ruthenium-nickel alloy nanowire electrocatalysts towards oxygen/hydrogen evolution reaction. *Int. J. Hydrogen Energy* **2022**, *47*, 31330. [[CrossRef](#)]
18. Zhou, P.; Tao, L.; Tao, S.; Li, Y.; Wang, D.; Dong, X.; Frauenheim, T.; Fu, X.; Lv, X.; Wang, S. Construction of Nickel-Based Dual Heterointerfaces towards Accelerated Alkaline Hydrogen Evolution via Boosting Multi-Step Elementary Reaction. *Adv. Funct. Mater.* **2021**, *31*, 2104827. [[CrossRef](#)]
19. Baek, D.S.; Lim, H.Y.; Kim, J.; Lee, J.; Lim, J.S.; Kim, D.; Lee, J.H.; Jang, J.W.; Kwak, S.K.; Joo, S.H. Volcanic-Size-Dependent Activity Trends in Ru-Catalyzed Alkaline Hydrogen Evolution Reaction. *ACS Catal.* **2023**, *13*, 13638. [[CrossRef](#)]
20. Liu, X.; Song, X.; Jiang, G.; Tao, L.; Jin, Z.; Li, F.; He, Y.; Dong, F. Pt Single-Atom collaborate with Pt Atom-Clusters by an In-Situ confined strategy for accelerating electrocatalytic hydrogen evolution. *Chem. Eng. J.* **2024**, *481*, 148430. [[CrossRef](#)]
21. Qian, M.; Liu, X.; Cui, S.; Jia, H.; Du, P. Copper oxide nanosheets prepared by molten salt method for efficient electrocatalytic oxygen evolution reaction with low catalyst loading. *Electrochim. Acta* **2018**, *263*, 318. [[CrossRef](#)]
22. Wang, J.; Liao, T.; Wei, Z.; Sun, J.; Guo, J.; Sun, Z. Heteroatom-Doping of Non-Noble Metal-Based Catalysts for Electrocatalytic Hydrogen Evolution: An Electronic Structure Tuning Strategy. *Small Methods* **2021**, *5*, 2000988. [[CrossRef](#)] [[PubMed](#)]
23. Yang, J.; Yang, S.; An, L.; Zhu, J.; Xiao, J.; Zhao, X.; Wang, D. Strain-Engineered Ru-NiCr LDH Nanosheets Boosting Alkaline Hydrogen Evolution Reaction. *ACS Catal.* **2024**, *14*, 3466. [[CrossRef](#)]
24. Zhu, T.; Han, J.; Sun, T.; Zhao, J.; Pi, X.; Xu, J.; Chen, K. Amorphous Ruthenium–Selenium Nanoparticles as a pH-Universal Catalyst for Enhanced Hydrogen Evolution Reaction. *ACS Catal.* **2024**, *14*, 1914. [[CrossRef](#)]
25. Cheng, R.; Min, Y.; Li, H.; Fu, C. Electronic structure regulation in the design of low-cost efficient electrocatalysts: From theory to applications. *Nano Energy* **2023**, *115*, 108718. [[CrossRef](#)]
26. Cai, W.; Zhou, C.; Hu, X.; Jiao, T.; Liu, Y.; Li, L.; Li, J.; Kitano, M.; Hosono, H.; Wu, J. Quasi-Two-Dimensional Intermetallic Electride CeRuSi for Efficient Alkaline Hydrogen Evolution. *ACS Catal.* **2023**, *13*, 4752. [[CrossRef](#)]
27. Chu, X.; Wang, L.; Li, J.; Xu, H. Strategies for Promoting Catalytic Performance of Ru-Based Electrocatalysts towards Oxygen/Hydrogen Evolution Reaction. *Chem. Rec.* **2023**, *23*, e202300013. [[CrossRef](#)]
28. Wen, Y.; Chen, P.; Wang, L.; Li, S.; Wang, Z.; Abed, J.; Mao, X.; Min, Y.; Dinh, C.T.; Luna, P.D.; et al. Stabilizing Highly Active Ru Sites by Suppressing Lattice Oxygen Participation in Acidic Water Oxidation. *J. Am. Chem. Soc.* **2021**, *143*, 6482. [[CrossRef](#)]
29. Wang, J.; Guo, B.; Sun, J.; Zhou, Y.; Zhao, C.; Wei, Z.; Guo, J. Cooperative hydrogen evolution reaction combining Cu₂₊₁O and Ru active sites. *Appl. Catal. B Environ.* **2023**, *324*, 122169. [[CrossRef](#)]
30. Gao, F.; Wang, Y.; Wang, S. Selective adsorption of CO on CuCl/Y adsorbent prepared using CuCl₂ as precursor: Equilibrium and thermodynamics. *Chem. Eng. J.* **2016**, *290*, 418. [[CrossRef](#)]
31. Xu, J.; Chen, C.; Kong, X. Ru–O–Cu center constructed by catalytic growth of Ru for efficient hydrogen evolution. *Nano Energy* **2023**, *111*, 108403. [[CrossRef](#)]
32. Xi, W.; Jin, L.; Mahmood, A.; Zhang, W.; Li, Y.; Li, H.; An, P.; Zhang, J.; Ma, T.; Liu, S.; et al. Accelerating Ru⁰/Ru⁴⁺ Adjacent Dual Sites Construction by Copper Switch for Efficient Alkaline Hydrogen Evolution. *Adv. Energy Mater.* **2023**, *13*, 2302668. [[CrossRef](#)]
33. Ren, D.; Deng, Y.; Handoko, A.D.; Chen, C.S.; Malkhandi, S.; Yeo, B.S. Selective Electrochemical Reduction of Carbon Dioxide to Ethylene and Ethanol on Copper(I) Oxide Catalysts. *ACS Catal.* **2015**, *5*, 2814. [[CrossRef](#)]
34. Zhu, J.; Lu, R.; Shi, W.; Gong, L.; Chen, D.; Wang, P.; Chen, L.; Wu, J.; Mu, S.; Zhao, Y. Epitaxially Grown Ru Clusters–Nickel Nitride Heterostructure Advances Water Electrolysis Kinetics in Alkaline and Seawater Media. *Energy Environ. Mater.* **2023**, *6*, e12318. [[CrossRef](#)]
35. Cai, J.; Zhang, W.; Liu, Y.; Shen, R.; Xie, X.; Tian, W.; Zhang, X.; Ding, J.; Liu, Y.; Li, B. Interfacial synergistic effect of Ru nanoparticles embedded onto amorphous/crystalline WO₃ nanorods on boosting the pH-universal hydrogen evolution reaction. *Appl. Catal. B Environ.* **2024**, *343*, 123502. [[CrossRef](#)]
36. Silitonga, M.Z.; Gultom, N.S.; Kuo, D.H. A novel approach to enhancing hydrogen evolution efficiency and durability: Bilayer metallic adhesion engineering in Ni/CoNi₄ film cathode. *Appl. Surf. Sci.* **2024**, *655*, 159651. [[CrossRef](#)]

37. Yoon, Y.; Lim, S.; Lim, T. Rational design of CoMoP heterostructure on Cu nanowires for enhanced electrocatalytic hydrogen evolution in alkaline and acidic media. *Int. J. Hydrog. Energy* **2024**, *59*, 107. [[CrossRef](#)]
38. Wang, S.; Xu, B.; Huo, W.; Feng, H.; Zhou, X.; Fang, F.; Xie, Z.; Shang, J.K.; Jiang, J. Efficient FeCoNiCuPd thin-film electrocatalyst for alkaline oxygen and hydrogen evolution reactions. *Appl. Catal. B Environ.* **2022**, *313*, 121472. [[CrossRef](#)]
39. Ma, S.; Yang, P.; Chen, J.; Wu, Z.; Li, X.; Zhang, H. NiCu alloys anchored Co₃O₄ nanowire arrays as efficient hydrogen evolution electrocatalysts in alkaline and neutral media. *J. Colloid Interface Sci.* **2023**, *642*, 604. [[CrossRef](#)]
40. Zhang, X.-Y.; Yu, W.-L.; Zhao, J.; Dong, B.; Liu, C.-G.; Chai, Y.-M. Recent development on self-supported transition metal-based catalysts for water electrolysis at large current density. *Appl. Mater. Today* **2021**, *22*, 100913. [[CrossRef](#)]
41. Kong, X.; Xu, J.; Ju, Z.; Chen, C. Durable Ru Nanocrystal with HfO₂ Modification for Acidic Overall Water Splitting. *Nano-Micro Lett.* **2024**, *16*, 185. [[CrossRef](#)] [[PubMed](#)]
42. Gultom, N.S.; Chang, L.H.; Silitonga, M.Z.; Ha, Q.N.; Janitra, R.S.; Kuo, D.H. Highly effective hydrogen evolution reaction in alkaline conditions using a sputtered bimetal Ni-Mo system: Experimental and computational evidence. *J. Alloys Compd.* **2024**, *1002*, 175406. [[CrossRef](#)]
43. Li, W.; Liu, J.; Guo, P.; Li, H.; Fei, B.; Guo, Y.; Pan, H.; Sun, D.; Fang, F.; Wu, R. Co/CoP Heterojunction on Hierarchically Ordered Porous Carbon as a Highly Efficient Electrocatalyst for Hydrogen and Oxygen Evolution. *Adv. Energy Mater.* **2021**, *11*, 2102134. [[CrossRef](#)]
44. Jeong, H.; Jang, H.; Kim, Y.H.; Kim, M.; Kang, Y.; Myung, J.-H. Surface exsolved NiFeOx nanocatalyst for enhanced alkaline oxygen evolution catalysis. *Appl. Surf. Sci.* **2024**, *662*, 160134. [[CrossRef](#)]
45. Liu, T.; Guan, Y.; Wu, Y.; Chu, X.; Liu, B.; Zhang, N.; Liu, C.; Jiang, W.; Che, G. Ru nanoparticles immobilized on self-supporting porphyrinic MOF/nickel foam electrode for efficient overall water splitting. *Int. J. Hydrog. Energy* **2024**, *57*, 408. [[CrossRef](#)]
46. Cao, D.; Huang, X.; Zhang, H.; Liu, W.; Cheng, D. Constructing porous RuCu nanotubes with highly efficient alloy phase for water splitting in different pH conditions. *Chem. Eng. J.* **2023**, *456*, 141148. [[CrossRef](#)]
47. Wu, Y.; Yao, R.; Zhang, K.; Zhao, Q.; Li, J.; Liu, G. RuO₂/CeO₂ heterostructure anchored on carbon spheres as a bifunctional electrocatalyst for efficient water splitting in acidic media. *Chem. Eng. J.* **2024**, *479*, 147939. [[CrossRef](#)]
48. Zhang, R.; Wang, X.; Yu, S.J.; Wen, T.; Zhu, X.W.; Yang, F.X.; Sun, X.N.; Wang, X.K.; Hu, W.P. Ternary NiCo₂P_x Nanowires as pH-Universal Electrocatalysts for Highly Efficient Hydrogen Evolution Reaction. *Adv. Mater.* **2017**, *29*, 1605502. [[CrossRef](#)]
49. Yan, L.; Yan, L.; Zhang, B.; Zhu, J.; Li, Y.; Tsiakaras, P.; Shen, P.K. Electronic modulation of cobalt phosphide nanosheet arrays via copper doping for highly efficient neutral-pH overall water splitting. *Appl. Catal. B Environ.* **2020**, *265*, 118555. [[CrossRef](#)]
50. Liu, T.; Ma, X.; Liu, D.; Hao, S.; Du, G.; Ma, Y.; Asir, A.M.; Sun, X.; Chen, L. Mn Doping of CoP Nanosheets Array: An Efficient Electrocatalyst for Hydrogen Evolution Reaction with Enhanced Activity at All pH Values. *ACS Catal.* **2017**, *7*, 98–102. [[CrossRef](#)]
51. Gao, X.; Chen, Y.; Sun, T.; Huang, J.; Zhang, W.; Wang, Q.; Cao, R. Karst landform-featured monolithic electrode for water electrolysis in neutral media. *Energy Environ. Sci.* **2020**, *13*, 174–182. [[CrossRef](#)]
52. Zeng, L.; Zeng, L.Y.; Sun, K.A.; Chen, Y.J.; Liu, Z.; Chen, Y.J.; Pan, Y.; Zhao, R.Y.; Liu, Y.Q.; Liu, C.G. Neutral-pH overall water splitting catalyzed efficiently by a hollow and porous structured ternary nickel sulfoselenide electrocatalyst. *J. Mater. Chem. A* **2019**, *7*, 16793–16802. [[CrossRef](#)]
53. Feng, J.X.; Feng, J.X.; Xu, H.; Ye, S.H.; Ouyang, G.F.; Tong, Y.X.; Li, G.R. Silica–Polypyrrole Hybrids as High-Performance Metal-Free Electrocatalysts for the Hydrogen Evolution Reaction in Neutral Media. *Angew. Chem. Int. Ed.* **2017**, *56*, 8120–8124. [[CrossRef](#)] [[PubMed](#)]
54. Xie, X.; Xie, X.H.; Song, M.; Wang, L.G.; Engelhard, M.H.; Luo, L.L.; Miller, A.; Zhang, Y.Y.; Du, L.; Pan, H.L.; et al. Electrocatalytic Hydrogen Evolution in Neutral pH Solutions: Dual-Phase Synergy. *ACS Catal.* **2019**, *9*, 8712–8718. [[CrossRef](#)]
55. Li, Q.; Huang, F.Z.; Li, S.K.; Zhang, H.; Yu, X.Y. Oxygen Vacancy Engineering Synergistic with Surface Hydrophilicity Modification of Hollow Ru Doped CoNi-LDH Nanotube Arrays for Boosting Hydrogen Evolution. *Small* **2022**, *18*, 2104323. [[CrossRef](#)]
56. Wang, J.; Fang, W.H.; Hu, Y.; Zhang, Y.H.; Dang, J.Q.; Wu, Y.; Chen, B.Z.; Zhao, H.; Li, Z.X. Single atom Ru doping 2H-MoS₂ as highly efficient hydrogen evolution reaction electrocatalyst in a wide pH range. *Appl. Catal. B Environ.* **2021**, *298*, 120490. [[CrossRef](#)]
57. Zhou, S.; Jang, H.; Qin, Q.; Li, Z.J.; Kim, M.G.; Ji, X.Q.; Liu, X.; Cho, J. Ru atom-modified Co₄N-CoF₂ heterojunction catalyst for high-performance alkaline hydrogen evolution. *Chem. Eng. J.* **2021**, *414*, 128865. [[CrossRef](#)]
58. Zhi, Q.; Qin, S.B.; Liu, W.P.; Jiang, R.; Sun, T.T.; Wang, K.; Jin, P.; Jiang, J.Z. Ultralow loading of ruthenium nanoparticles on nitrogen-doped porous carbon enables ultrahigh mass activity for the hydrogen evolution reaction in alkaline media. *Catal. Sci. Technol.* **2021**, *11*, 3182–3188. [[CrossRef](#)]
59. Li, P.; Duan, X.X.; Wang, S.Y.; Zheng, L.R.; Li, Y.P.; Duan, H.H.; Kuang, Y.; Sun, X.M. Amorphous Ruthenium-Sulfide with Isolated Catalytic Sites for Pt-Like Electrocatalytic Hydrogen Production Over Whole pH Range. *Small* **2019**, *15*, 1904043. [[CrossRef](#)]
60. Zhu, Y.; Tahini, H.A.; Hu, Z.W.; Dai, J.; Chen, Y.B.; Sun, H.N.; Zhou, W.; Liu, M.L.; Smith, S.C.; Wang, H.T.; et al. Unusual synergistic effect in layered Ruddlesden–Popper oxide enables ultrafast hydrogen evolution. *Nat. Commun.* **2019**, *10*, 149. [[CrossRef](#)]

61. Zhang, X.Y.; Zhu, Y.R.; Chen, Y.; Dou, S.Y.; Chen, X.Y.; Dong, B.; Guo, B.Y.; Liu, D.P.; Liu, C.G.; Chai, Y.M. Hydrogen evolution under large-current-density based on fluorine-doped cobalt-iron phosphides. *Chem. Eng. J.* **2020**, *399*, 125831. [[CrossRef](#)]
62. Zheng, Y.; Jiao, Y.; Zhu, Y.H.; Li, L.H.; Han, Y.; Chen, Y.; Jaroniec, M.; Qiao, S.Z. High Electrocatalytic Hydrogen Evolution Activity of an Anomalous Ruthenium Catalyst. *J. Am. Chem. Soc.* **2016**, *138*, 16174–16181. [[CrossRef](#)]
63. Liu, H.; Xia, G.L.; Zhang, R.R.; Jiang, P.; Chen, J.T.; Chen, Q.W. MOF-derived RuO₂/Co₃O₄ heterojunctions as highly efficient bifunctional electrocatalysts for HER and OER in alkaline solutions. *RSC Adv.* **2017**, *7*, 3686–3694. [[CrossRef](#)]
64. Liu, X.; Liu, F.; Yu, J.Y.; Xiong, G.W.; Zhao, L.L.; Sang, Y.H.; Zuo, S.W.; Zhang, J.; Liu, H.; Zhou, W.J. Charge Redistribution Caused by S,P Synergistically Active Ru Endows an Ultrahigh Hydrogen Evolution Activity of S-Doped RuP Embedded in N,P,S-Doped Carbon. *Adv. Sci.* **2020**, *7*, 2001526. [[CrossRef](#)] [[PubMed](#)]
65. Yan, B.; Liu, D.P.; Feng, X.L.; Shao, M.Z.; Zhang, Y. Ru Species Supported on MOF-Derived N-Doped TiO₂/C Hybrids as Efficient Electrocatalytic/Photocatalytic Hydrogen Evolution Reaction Catalysts. *Adv. Funct. Mater.* **2020**, *30*, 2003007. [[CrossRef](#)]
66. Feng, P.; Wang, P.Y.; Qin, R.; Shi, W.J.; Gong, L.; Zhu, J.W.; Ma, Q.L.; Chen, L.; Yu, J.; Liu, S.L.; et al. Flower-Like Amorphous MoO_{3-x} Stabilized Ru Single Atoms for Efficient Overall Water/Seawater Splitting. *Adv. Sci.* **2023**, *10*, 2300342. [[CrossRef](#)]
67. Jiang, R.; Da, Y.M.; Zhang, J.F.; Wu, H.; Fan, B.B.; Li, J.H.; Wang, J.J.; Deng, Y.D.; Han, X.P.; Hu, W.B. Non-equilibrium synthesis of stacking faults-abundant Ru nanoparticles towards electrocatalytic water splitting. *Appl. Catal. B* **2022**, *316*, 121682. [[CrossRef](#)]
68. Chen, D.; Yu, R.H.; Wu, D.L.; Zhao, H.Y.; Wang, P.Y.; Zhu, J.W.; Ji, P.X.; Pu, Z.H.; Chen, L.; Yu, J.; et al. Anion-modulated Molybdenum Oxide Enclosed Ruthenium Nano-capsules with Almost the Same Water Splitting Capability in Acidic and Alkaline Media. *Nano Energy* **2022**, *100*, 107445. [[CrossRef](#)]
69. Qin, R.; Wang, P.Y.; Li, Z.L.; Zhu, J.X.; Cao, F.; Xu, H.W.; Ma, Q.L.; Zhang, J.Y.; Yu, J.; Mu, S.C. Ru-incorporated Nickel Diselenide Nanosheet Arrays with Accelerated Adsorption Kinetics toward Overall Water Splitting. *Small* **2022**, *18*, 2105305. [[CrossRef](#)]
70. Liu, D.; Xu, H.; Wang, C.; Ye, C.Q.; Yu, R.; Du, Y.K. In situ etch engineering of Ru doped NiFe(OH)_x/NiFe-MOF nanocomposites for boosting the oxygen evolution reaction. *J. Mater. Chem. A* **2021**, *9*, 24670–24676. [[CrossRef](#)]
71. Zhao, J.; Zhang, Y.Y.; Xia, Y.Z.; Zhang, B.; Du, Y.C.; Song, B.; Wang, H.L.; Li, S.W.; Xu, P. Strong phosphide-metaphosphate interaction in RuP/CoNiP₄O₁₂ for enhanced electrocatalytic water splitting. *Appl. Catal. B* **2023**, *328*, 122447. [[CrossRef](#)]
72. Liu, D.; Xu, H.; Wang, C.; Shang, H.Y.; Yu, R.; Wang, Y.; Li, J.; Li, X.C.; Du, Y.K. 3D Porous Ru-Doped NiCo-MOF Hollow Nanospheres for Boosting Oxygen Evolution Reaction Electrocatalysis. *Inorg. Chem.* **2021**, *60*, 5882–5889. [[CrossRef](#)]
73. Hao, Y.R.; Xue, H.; Sun, J.; Guo, N.K.; Song, T.S.; Sun, J.W.; Wang, Q. Tuning the Electronic Structure of CoP Embedded in N-Doped Porous Carbon Nanocubes Via Ru Doping for Efficient Hydrogen Evolution. *ACS Appl. Mater. Interfaces* **2021**, *13*, 56035–56044. [[CrossRef](#)] [[PubMed](#)]
74. You, M.; Du, X.; Hou, X.H.; Wang, Z.Y.; Zhou, Y.; Ji, H.P.; Zhang, L.Y.; Zhang, Z.T.; Yi, S.S.; Chen, D.L. In-situ growth of ruthenium-based nanostructure on carbon cloth for superior electrocatalytic activity towards HER and OER. *Appl. Catal. B* **2022**, *317*, 121729. [[CrossRef](#)]

Disclaimer/Publisher's Note: The statements, opinions and data contained in all publications are solely those of the individual author(s) and contributor(s) and not of MDPI and/or the editor(s). MDPI and/or the editor(s) disclaim responsibility for any injury to people or property resulting from any ideas, methods, instructions or products referred to in the content.